THE JOURNAL OF PHYSICAL CHEMISTRY A
A JOURNAL OF THE AMERICAN CHEMICAL SOCIETY

pubs.acs.org/JPCA Article

Hydration and Hydrogen Bond Order of Octadecanoic Acid and Octadecanol Films on Water at 21 and 1 °C

Published as part of The Journal of Physical Chemistry virtual special issue "125 Years of The Journal of Physical Chemistry".

Maria G. Vazquez de Vasquez,[§] Kimberly A. Carter-Fenk,[§] Laura M. McCaslin, Emma E. Beasley, Jessica B. Clark, and Heather C. Allen*

Cite This: https://doi.org/10.1021/acs.jpca.1c06101 Read Online

ACCESS | Metrics & More | Article Recommendations | Supporting Information

ABSTRACT: The temperature-dependent hydration structure of long-chain fatty acids and alcohols at air−water interfaces has great significance in the fundamental interactions underlying ice nucleation in the atmosphere. We present an integrated theoretical and experimental study of the temperature-dependent vibrational structure and electric field character of the immediate hydration shells of fatty alcohol and acid headgroups. We use a combination of surface-sensitive infrared reflection−absorption spectroscopy (IRRAS), surface potentiometry, and *ab initio* molecular dynamics simulations to elucidate detailed molecular structures of the octadecanoic acid and octadecanol (stearic acid and stearyl alcohol) headgroup hydration shells at room temperature and near freezing. In experiments, the alcohol at high surface concentration exhibits the largest surface potential; yet we observe a strengthening of the hydrogen-bonding for the solvating water molecules near freezing for both the alcohol and the fatty acid IRRAS experiments. Results reveal that the hydration shells for both compounds screen their polar headgroup dipole moments reducing the surface potential at low surface coverages; at higher surface coverage, the polar headgroups become dehydrated, which reduces the screening, correlating to higher observed surface potential values. Lowering the temperature promotes tighter chain packing and an increase in surface potential. IRRAS reveals that the intra- and intermolecular vibrational coupling mechanisms are highly sensitive to changes in temperature. We find that intramolecular coupling dominates the vibrational relaxation pathways for interfacial water determined by comparing the H_2O and the HOD spectra. Using *ab initio* molecular dynamics (AIMD) calculations on cluster systems of propanol + $6H_2O$ and propionic acid + $10H_2O$, a spectral decomposition scheme was used to correlate the OH stretching motion with the IRRAS spectral features, revealing the effects of intra- and intermolecular coupling on the spectra. Spectra calculated with AIMD reproduce the red shift and increase in intensity observed in experimental spectra corresponding to the OH stretching region of the first solvation shell. These findings suggest that intra- and intermolecular vibrational couplings strongly impact the OH stretching region at fatty acid and fatty alcohol water interfaces. Overall, results are consistent with ice templating behavior for both the fatty acid and the alcohol, yet the surface potential signature is strongest for the fatty alcohol. These findings develop a better understanding of the complex surface potential and spectral signatures involved in ice templating.

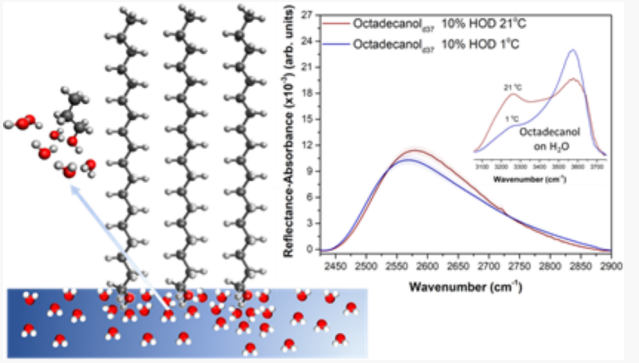

1. INTRODUCTION

Fatty alcohol and fatty acid monolayers are highly relevant in ocean surface chemistry, aerosols, ice nucleation in clouds, oil recovery, and biomembranes, though studies of their hydration and surface potential properties at low temperatures are limited. Garrett et al. showed that the major organic constituents of the ocean surface are high molecular weight molecules with low water solubility, such as fatty alcohols and acids.[1] Surface activity of these fatty compounds is well established such that they congregate at aqueous surfaces. While the favorable ice nucleation properties of fatty alcohols are well accepted, recent evidence suggests that, at cooler temperatures, long chain fatty acids from the sea surface microlayer are active in the ice nucleation process.[2,3] It has been shown through molecular simulations and laboratory

Received: July 8, 2021
Revised: October 28, 2021

experiments that ice nucleation efficiency is increased by good structural matching of the hydrogen-bonding structure of water around a fatty alcohol interface to that of bulk ice.[3] This structural matching is well-known as ice templating, where theoretical studies have linked the freezing behavior to the 2D structure at the water interface.[3] In addition to ice nucleation processes, these fatty compounds are also key components in biomembranes and play a role in chemically enhanced oil recovery.[4] To develop more detailed models for the formation of monolayer and bilayers and their biological functions, Serafin et al. showed that phospholipid−fatty alcohol complexes can stably form at the air−water interface.[5]

Although research on hydration of fatty acid and alcohols is limited, recent spectroscopic work of the solvation structure of both dilute and concentrated short-and medium chain linear alcohols in solution as a function of temperature is notable.[6−10] Davis et al., using Raman scattering measurements, showed that very dilute alcohol solutions at temperatures just above 0 °C promote ordering of the surrounding hydrogen-bond network of water, whereas increasing temperature or alcohol chain length was shown to disrupt the ordering of the hydration shell.[7] These solution Raman studies were later confirmed by Deng et al. using IR-spectroscopy measurements also revealing changes in the tetrahedral water structure of the hydration shell.[10] In addition to solution-based studies, cluster and molecular simulation approaches provide an important picture on the hydrogen-bonding network in aqueous solutions.[11−16] Previously, it has been shown that three to four water molecules are in direct contact with the OH ion in aqueous solution.[11−13,17] Fujii et al. showed that small protonated methanol clusters undergo a phase change borne out in the hydrogen-bonding structure with temperature elevation.[17] Additionally, a study on freezing behavior of aqueous-alcohol nanodroplets as a function of alcohol concentration showed that nucleation occurs throughout the volume of the nanodroplet (bulk) rather than at or near its surface.[18]

Understanding hydration of monolayers and how differences in microenvironment can affect the hydrogen bond network has been of particular interest for many years.[19−24] In 1993 Alper and coauthors studied the behavior of water hydration in a phospholipid monolayer. Their results revealed rapid water motion yet preferential ordering with three hydration shells about the lipid phosphocholine group with a clathrate-like hydration structure around the choline.[19] Several studies of water in reverse micelles have been used to describe nano confined water and to obtain information regarding perturbations to the hydrogen bond network using a core−shell model. The core−shell model consists of a bulk water component and an interfacial water component for all reverse micelle sizes. This model suggests that the core water molecules would not be substantially affected by the interface.[25,26] Such studies demonstrated that confinement significantly affects the hydrogen bond network evolution of water in small reverse micelles.[20,21] While interfacial and confining environments are not necessarily the same, they both provide important information on the hydrogen-bonding network. The core−shell model of water dynamics were subdivided into two main contributions, a shell region corresponding to the water molecules strongly associated with the lipid headgroups and a core region consisting of water molecules positioned away from the headgroup that possess bulk-like properties.[22] Structure and dynamics understanding of liquid water remains an important and challenging problem, in particular, in the interpretation of the OH stretch region since it is extremely sensitive to molecular environments. Studies argue that the intermolecular and intramolecular coupling make the interpretation of this region difficult.[27] Therefore, studies of isotopic dilution focusing on dilute HOD mitigates the effect of intramolecular and intermolecular vibrational coupling to other vibrational modes.[25−30] Moreover, the OD stretch of dilute HOD in H_2O is used to eliminate problems due to vibrational excitation transfer.[25]

Herein, we first evaluate and quantify the temperature-dependent hydration effects of two different fatty compound monolayers using interfacial surface pressure and surface potentiometry. Both techniques provide information on the overall monolayer structure and intermolecular interactions. Surface potentiometry provides information on dipole moment alignment of the compounds and their hydration shell. To reveal changes in hydration as a function of temperature, infrared reflection−absorption spectroscopy (IRRAS) is utilized to collect surface-sensitive infrared spectra of octadecanol (stearyl-d_{37} alcohol) and octadecanoic acid (stearic-d_{35} acid) monolayers at the air−water interface. IRRAS provides a unique advantage given that it only probes the monolayer and the hydration shell immediately perturbed by the presence of the compounds at the interface. We spectrally measure the OH stretching modes of the headgroups and their hydration shells as well as the HOH bending modes of the hydrating water molecules. We also examine the OD stretch of dilute HOD in H_2O to understand the impacts of vibrational excitation transfer. Additionally, to gain insights into the temperature-dependent vibrational structure of the headgroup and water molecules in the first solvation shell around alcohols and carboxylic acids, the IR spectra of the propanol + $6H_2O$ and propionic acid + $10H_2O$ are computed from *ab initio* molecular dynamics (AIMD) calculations. The temperature dependence of the spectra is then calculated using techniques from fluctuation theory. A spectral decomposition technique is introduced and used to correlate specific OH stretching motions to spectral features. Although, molecular dynamics studies on the changes in hydration structure around the headgroup at the monolayer interface have been previously performed, to our knowledge a study on changes in vibrational structure and transition moments with temperatures have not been conducted. Our experimental and theoretical calculations show that strong correlations between OH stretching modes play a significant role in the spectra, as well as coupling between OH stretching and H_2O bending modes. The IRRAS spectra suggest that these highly correlated interactions disrupt the water−water hydrogen-bonding network near freezing temperature. The spectral frequency shifts, however, show a red shift suggesting more ordered water molecules at lower temperatures. Our experiments in dilute 10% HOD in H_2O reveal the degree to which vibrational excitation transfer occurs in 100% H_2O underlining the role of intramolecular coupling.

2. EXPERIMENTAL AND COMPUTATIONAL METHODS

2.1. Materials. Octadecanoic acid (stearic acid, $CH_3(CH_2)_{16}COOH$,>99%, Sigma-Aldrich), octadecanol (stearyl alcohol, $CH_3(CH_2)_{17}OH$, 99%, Sigma-Aldrich), deuterated octadecanoic acid (stearic-d_{35} acid, $CD_3(CD_2)_{16}CO_2H$, > 98%, Sigma-Aldrich), and deuterated octadecanol (stearyl-d_{37} alcohol, $CD_3(CD_2)_{17}OH$, > 98%,

https://doi.org/10.1021/acs.jpca.1c06101
J. Phys. Chem. A XXXX, XXX, XXX−XXX

Cambridge Isotopes Laboratories) were used as received. The compounds were dissolved in chloroform (HPLC grade, Fisher Scientific) to prepare ∼3 mM octadecanoic acid and octadecanol solutions and ∼2 mM octadecanoic-d_{35} acid and octadecanol-d_{37} solutions. Control experiments were performed using a cationic surfactant, dimethyldioctadecylammonium (bromo salt, DDBA; > 98% Sigma-Aldrich). Nanopure water with a resistivity of 18.2 MΩ·cm (Milli-Q Advantage A10, EMD Millipore) and 5% deuterium oxide (D_2O, 99.9 atom % D, Sigma-Aldrich) in nanopure water were used as the aqueous subphases. The ultrapure water had a pH of 5.6 due to atmospheric CO_2 acidification and was equilibrated at room temperature prior to starting experiments.

2.2. Surface Pressure and Surface Potential−Area Isotherms. Surface pressure and surface potential−area isotherm experiments were conducted in triplicate using a Teflon Langmuir trough with Delrin barriers (KSV NIMA, Biolin Scientific, 549.08 cm^2 in surface area). Prior to a measurement, the trough and barriers were thoroughly cleaned with reagent alcohol (Histological grade, Fisher Scientific) and ultrapure water. The surface potential (SPOT, KSV NIMA) sensor was placed halfway along the length of the trough and about 1−2 mm above the water surface, leaving enough distance from the trough edges to reduce interference. The counter electrode was submerged in the subphase parallel to the vibrating probe surface. The SPOT sensor was allowed to equilibrate with its surroundings for at least 10 min before starting the first experiment. Surface pressure was measured using the Wilhelmy plate method with a filter paper plate (Ashless grade 41, Whatman, GE Healthcare) that was completely wetted prior to running a compression isotherm experiment. The trough was then filled with ultrapure water; surface cleanliness (surface pressure ≤0.20 mN/m) was verified by sweeping the barriers at a compression speed of 270 mm/min/barrier. Surface pressure and surface potential were then zeroed, and a microsyringe (Hamilton) was used to spread the surfactant solution dropwise onto the subphase. Ten minutes were allowed for solvent evaporation, followed by symmetrical and constant compression of the monolayer at a rate of 10 mm/min (5 mm/min/barrier). Surface pressure and surface potential−area isotherms were conducted at 21.0 °C and 1.0 ± 1.0 °C and a relative humidity of 35 ± 5%.

2.3. Infrared Reflection−Absorption Spectroscopy. Interface-sensitive infrared reflection−absorption spectroscopy (IRRAS) was used to spectrally evaluate the interfacial region. A custom-built setup was used and placed in the chamber of a Fourier transform infrared (FTIR) spectrometer (Frontier, PerkinElmer) with a liquid-nitrogen-cooled HgCdTe (MCT) detector. A Langmuir trough was set inside the spectrometer on a breadboard containing two gold mirrors. The first mirror directs the incoming unpolarized IR beam to the sample surface at a 48° incident angle relative to the surface normal. As some of the light is reflected off the water surface, it is directed by the second gold mirror toward the MCT detector. Each spectrum was collected as an average of 400 scans using a single-beam mode over the full spectral range of 4000−450 cm^{-1} at a 4 cm^{-1} setting. Data analysis was performed using Origin software (OriginLab 9). The spectra shown here are plotted as an average of at least three individual spectra. The OH stretching region spectra were individually baseline-subtracted using a line function between the end points 3800 and 2900 cm^{-1}, and the HOH bending mode spectra were baseline-subtracted by fitting a fourth order polynomial function along the baseline between 1900 and 1250 cm^{-1}. Spectra were collected at 21.0 °C and 1.0 ± 1.0 °C and a lab relative humidity of 35 ± 5%.

2.4. *Ab Initio* Molecular Dynamics. The first solvation shell around a model alcohol and a model fatty acid is studied using *ab initio* molecular dynamics (AIMD). The model alcohol system chosen is propanol (C_3H_7OH) + $6H_2O$. The model fatty acid system chosen is propionic acid (C_2H_2COOH) + $10H_2O$. Twenty AIMD trajectories for each of these systems are performed for 2 ps with a time step of 0.5 fs in the canonical (*NVT*) ensemble. The ωB97X-D functional is used in concert with the aug-cc-pVDZ basis to obtain energies, gradients, and dipole moments at each time step in the trajectories.[31,32] Initial velocities are sampled from a Boltzmann distribution at 300 K. A Nosé−Hoover thermostat at 300 K is employed with a chain length of 3 and a 100 fs time scale.[33] All AIMD calculations are performed in Q-Chem.[34] The IR spectra are computed by taking the Fourier transform of the autocorrelation function of the dipole moment.[35]

A spectral decomposition technique is presented based on the outer product of the Fourier transformed velocity vectors, forming the Θ tensor, as described in Mathias et al.[36] This object is made up of a $3N \times 3N$ matrix for each frequency in the Fourier transform, where N is the number of atoms and is the velocity cross correlation matrix in Cartesian coordinates. Previous studies have diagonalized this matrix for each frequency to identify the dominant molecular motion correlated with each frequency in order to characterize spectra with overlapping bands.[37] Here, however, we are interested in correlating spectral features with different OH stretches and their relative weights. In order to do this, we transform the Θ tensor into internal coordinates via multiplication by the Wilson B matrix.[38] This allows for the decomposition of each peak in internal coordinates, thus allowing for each spectral feature to be understood as the sum of the weight of each coordinate. Each spectral feature can be expressed as a sum of weights of sets of correlated internal coordinates, as discussed in Section 3.2.2 and Section 3.2.3. Further details on the calculation of these weights are given in the Supporting Information.

The temperature dependence of the IR spectra was computed using the techniques of fluctuation theory, as described in Piskulich et al.,[39] though the computation of the autocorrelation function in Piskulich et al. is adapted for condensed phase systems and differs from the techniques used in Q-Chem and thus this study, described in the Supporting Information. The IR spectra are computed from AIMD calculations at 300 K and scaled to obtain the intensities at 270 K. Previous studies accurately predicted the spectral shift in pure water systems for shifts of up to 60 K.[39] The frequencies in the calculated spectra in Sections 3.2.2 and 3.2.3 are scaled by a factor of 0.98212 to aid in comparison to experimental values. This factor was calculated to adjust the frequency corresponding to maximum intensity at 27 °C in the OH stretching region of propanol + $6H_2O$ (3644 cm^{-1}) to the experimental peak at 3581.5 cm^{-1}.

3. RESULTS AND DISCUSSION

3.1. Impacts of Temperature on Fatty Alcohol and Fatty Acid Monolayer Structure. To quantify the temperature-dependent hydration effects on monolayer structure, the organization of the monolayer is first probed via surface pressure−area isotherms in tandem with surface potentiom-

https://doi.org/10.1021/acs.jpca.1c06101
J. Phys. Chem. A XXXX, XXX, XXX−XXX

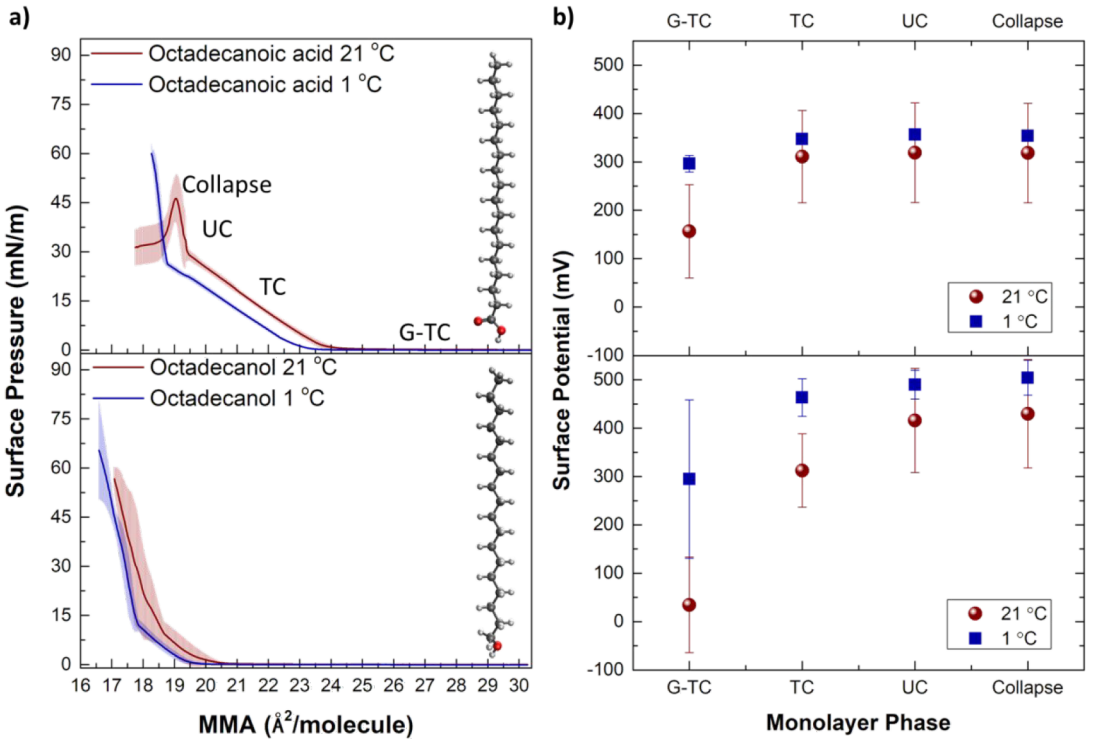

Figure 1. (a) Surface pressure isotherm of octadecanoic acid (top) and octadecanol (bottom) at 21.0 °C (red) and 1.0 ± 1.0 °C (blue) indicating the different phase transitions. (b) Surface potential changes of octadecanoic acid (top) and octadecanol (bottom) as a function of monolayer density at 21.0 °C (red) and 1.0 ± 1.0 °C (blue). Surface pressure and surface potential isotherm and exact MMAs used for each surface potential point can be found in the Figure S1 and Table S1.

etry, Figure 1. Both techniques provide insights on the overall monolayer structure and intermolecular interactions, and surface potentiometry provides semiquantitative information on dipole alignment of the compounds and their hydration shells.[40] Octadecanoic acid ($CH_3(CH_2)_{16}COOH$) and octadecanol ($CH_3(CH_2)_{17}OH$) were chosen to represent model sea spray aerosol films due to their marine-relevance and abundance in laboratory-generated nascent sea spray aerosol.[41] Both compounds have identical chain lengths and are neutrally charged (protonated) at pH 5.6, the pH of ultrapure water used in the experiments. Thus, the headgroup and its hydration structure drive the differences in the surface pressure−area isotherms and surface potential measurements.

All measurements were collected at both room temperature (21.0 ± 0.5 °C) and near freezing (1.0 ± 1.0 C) to represent a realistic range of temperatures experienced by sea spray aerosol in the atmosphere. Surface pressure−area isotherms near freezing have not been previously investigated, and prior studies have shown surface pressure data of fatty acids and fatty alcohols[42−44] at temperatures no lower than 5 °C.[42,45] Film studies have also measured the surface potential of both fatty alcohols and fatty acids to obtain organizational information, but not at lower temperatures.[43−49] These measurements were carried out to better understand the octadecanol and octadecanoic acid monolayer structural change and altered hydration environments at low temperatures.

At room temperature, our surface pressure−area isotherms closely match isotherms in the literature, Figure 1a.[41,44,50−56] As the barriers compress the octadecanol and octadecanoic acid monolayers to smaller mean molecular area (MMA), the films undergo a 2D phase transition. The first phase transition, known as the lift-off point, starts at the gas-tilted condensed (G-TC) coexistence region in which gaseous regions without aggregated fatty compounds coexist with small circular domains of aggregates in the TC phase. The monolayer transitions to the tilted condensed (TC) phase at 21 Å²/molecule for octadecanol and 24 Å²/molecule for octadecanoic acid, where the domains start to fuse together to form a fully condensed monolayer.[55,57−60] Upon further compression in the TC phase, the monolayers transition into the untilted condensed (UC) phase at 18.6 Å²/molecule for octadecanol and 19.5 Å²/molecule for octadecanoic acid. In this phase, the compounds are highly compressed and oriented nearly perpendicular to the water surface, causing the formation of a fully condensed film. Additionally, the octadecanol and octadecanoic acid films reach a maximum surface pressure observed at ∼57.5 and ∼47 mN/m, respectively. Hence, the octadecanol monolayer is more compressed relative to the octadecanoic acid monolayer across all two-dimensional phases due to the smaller spatial requirement for the alcohol headgroup in comparison to the larger carboxylic acid headgroup.

The surface pressure−area isotherms near freezing (1 °C) shown in Figure 1a are remarkably similar in shape to the room temperature isotherms, but there are some clear differences in the isotherm phase transitions. Octadecanol and octadecanoic acid monolayers lift-off at 20 and 23 Å²/molecule, respectively, decreasing the lift-off points by 1 Å²/molecule relative to the values at room temperature. The phase transition from the TC to the UC phase occurs at 17.8 Å²/molecule for octadecanol and at 18.8 Å²/molecule for octadecanoic acid, 0.8 Å²/molecule smaller relative to the MMA values for both compounds at room temperature. Moreover, the octadecanol

https://doi.org/10.1021/acs.jpca.1c06101
J. Phys. Chem. A XXXX, XXX, XXX−XXX

and octadecanoic acid films reach a maximum surface pressure at ~64.4 and ~59.8 mN/m, respectively, approximately 10 mN/m higher than the maximum monolayer surface pressures at room temperature. Thus, low temperature promotes tighter compression of both monolayers. Additionally, the lowered temperature has a nearly identical effect on the magnitude of MMA shifts in the isotherms for octadecanol and octadecanoic acid, suggesting that the magnitude of compression upon lowering the temperature is about the same for both compounds.

To gain more insight on monolayer organization and headgroup hydration, surface-sensitive surface potential measurements were obtained during monolayer compression. Surface potential is a technique that measures electrical properties of bare and surfactant-covered aqueous interfaces.[41] In these experiments, surface potential is measured as the difference in voltage from a clean water surface. The hydrophobic tail, polar headgroup, and composition of the underlying aqueous subphase all strongly influence the surface potential measurements.[43,47−49,61−64] Surface potential variation during monolayer compression is often discussed in terms of changes in dipole moment alignment due to tail orientation relative to the water surface; however, increasing molecular density and polar headgroup orientation and dehydration during monolayer compression are also important contributors to the overall surface potential.[65] Quadrupole contributions have also been indicated in some systems.[66] The headgroup hydration shells screen the polar headgroup dipole moments, thereby reducing the surface potential at large MMAs. Monolayer compression to low MMAs dehydrates the polar headgroups, reduces the dipole moment screening, and the increases surface potential.[65]

Figure 1b shows the surface potential response obtained for the three different octadecanol (bottom) and octadecanoic acid (top) monolayer phases (G-TC, TC, and UC). Our results show that the surface potential becomes nonzero and increases in magnitude in the G-TC coexistence phase (larger MMA values than the lift-off points in the surface pressure−area isotherms) for both octadecanol and octadecanoic acid at room temperature and near freezing. This suggests that domains form throughout compression in the G-TC coexistence phase, resulting in a positive surface potential value even when the surface pressure remains at zero prior to transition into the TC phase. Dehydration of the headgroups is also likely. At room temperature, octadecanoic acid has a surface potential of 157 ± 97 mV in the G-TC phase, and octadecanol has a surface potential of 35 ± 99 mV. One can argue that octadecanoic acid has a higher surface potential than octadecanol in this coexistence region due to a larger number on molecules existing in the TC phase thus less dipole moment screening of hydrating water molecules leading to an increase in dipole moment contribution from the carbonyl headgroup. Also, the octadecanoic acid tail may orient differently in the TC region relative to the alcohol due to its larger headgroup leading to less shielding and thus more exposure of the headgroup dipole moment.

Cooling-induced changes in the G-TC coexistence phase could play an important role in ice nucleation due to water molecule reorientation within the headgroup region to form ice-like structures.[3,41] It is interesting to note that the greatest magnitude of surface potential change between room temperature and near freezing occurs for octadecanol in the G-TC phase. At 1.0 °C, the octadecanoic acid surface potential is 296 ± 17 mV, and the octadecanol surface potential is 295 ± 164 mV. Thus, the difference between the 1 and 21 °C surface potential values in the G-TC phase for octadecanoic acid is 140 ± 98 mV, whereas the difference for octadecanol is 260 ± 192 mV. Our results suggest that octadecanol undergoes the greatest extent of headgroup hydration reorganization in the G-TC coexistence phase near freezing.

As the monolayer is compressed, the surface potential increases for both compounds until a maximum value is reached in the fully condensed UC phase. Thus, the rising surface potential shows increasing interfacial molecular density, enhanced ordering, and headgroup dehydration within the monolayer. The maximum surface potential values for octadecanol and octadecanoic acid on water at 21.0 °C are 429 ± 112 and 318 ± 103 mV, respectively, which agree with reported literature values of ~400−338 mV for octadecanol[43,46,47,61] and 280−380 mV for octadecanoic acid.[46−49,54,61,67−69] The maximum surface potential response for octadecanol was 111 ± 152 mV greater than the maximum value measured for octadecanoic acid, possibly due to octadecanol's strong C−OH dipole moment alignment at the interface and to the reorganization and structuring of water molecules adjacent to the headgroup. The orientation of the fatty tails affects the orientation of the headgroup and thus the water molecules at the interface.[48]

Temperature-dependent differences in surface potential are less significant in the UC phase as compared to phases with lower surface coverage, like the G-TC coexistence phase. An octadecanoic acid monolayer at 1 °C in the UC phase has a surface potential of 354 ± 7 mV, and an octadecanol monolayer has a surface potential of 504 ± 36 mV. The difference between the surface potential at 1 and 21 °C is 36 ± 103 mV for octadecanoic acid and 75 ± 109 mV for octadecanol. These fatty compounds have minimal room for rearrangement at high surface coverage due to both van der Waals interactions and dipole repulsion.[65]

3.2. Vibrational Spectroscopic Signatures of the Headgroups and Hydration Shells. To elucidate changes in hydration structure as a function of temperature, IRRAS spectroscopy was used to collect surface-sensitive infrared spectra of octadecanol-d_{37} and octadecanoic-d_{35} acid monolayers at the air−aqueous interface. Deuterated fatty compounds were selected to avoid spectral overlap of the carboxylic acid vibrational modes with the CH_2 scissoring modes. IRRAS spectra are plotted as reflectance−absorbance (RA),

$$\mathrm{RA} = -\log \frac{R_f}{R_0} \tag{1}$$

in which R_f corresponds to the reflectance of the film and R_0 corresponds to the reflectance of the bare water surface. Hence, only a reflected signal corresponding to the monolayer and its hydration shell is detected. Both positive and negative peaks are observable in our IRRAS spectra; the reflectance−absorbance values are negative when the film reflectance is greater than the water reflectance ($R_f/R_0 > 1$), and the reflectance−absorbance values are positive when the reflected signal from water is greater than that of the film ($R_f/R0 < 1$). In our spectra, the negative peaks correspond to monolayer vibrational modes, and the positive peaks correspond to the hydration shell modes. This observation is consistent with other published IRRAS spectra collected at IR beam angles of

https://doi.org/10.1021/acs.jpca.1c06101
J. Phys. Chem. A XXXX, XXX, XXX−XXX

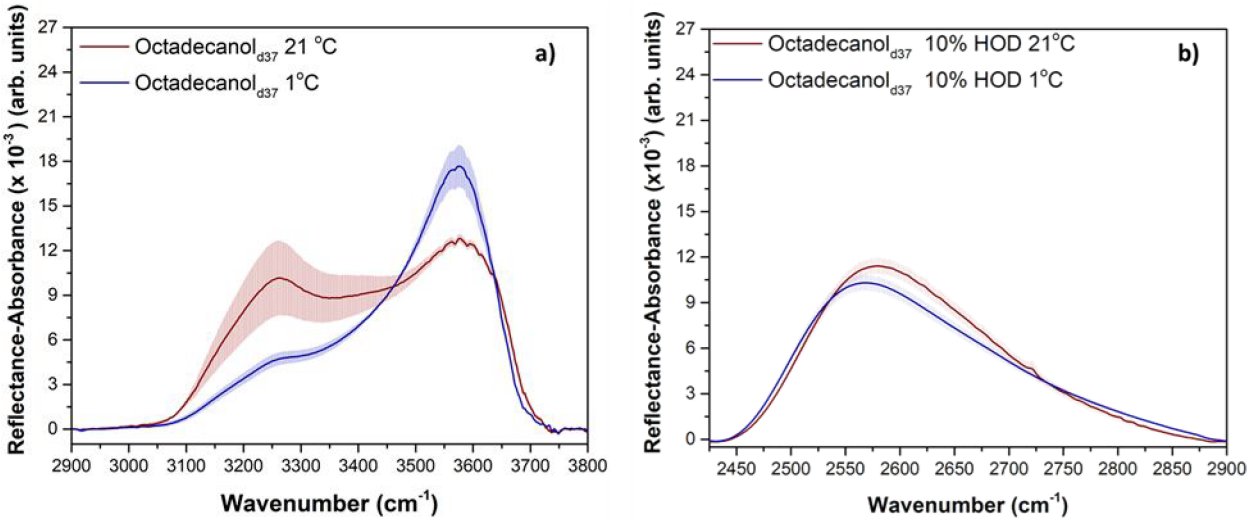

Figure 2. IRRAS spectra of the ν(OH) and ν(OD). (a) octadecanol-d_{37} alcohol illustrates the main ν(OH) bands one at 3600 cm^{-1}, typically attributed to the OH stretch of the groups weakly interacting with the neighbors and a 3250 cm^{-1} band due to strong interacting solvent (water) molecules at 21 ± 1 (red) and 1 ± 1 °C (blue). (b) OD spectral region of octadecanol-d_{37} in 5% D_2O in water (10% HOD). The ν(OD) is decoupled from the OH oscillators. The ν(OD) change in frequency (~10 cm^{-1} red shift) with temperature can be found Table S6.

incidence less than the Brewster angle of water (~53.1° relative to surface normal).[70−81]

Octadecanol-d_{37} and octadecanoic-d_{35} acid IRRAS spectra were collected at a surface pressure (Π) of 40 mN/m, which corresponds to the UC phase of the monolayers. To directly compare peak intensities between the spectra of the two compounds, an additional scaling factor is required to account for differences in film surface density at constant surface pressure. The scaling factor is calculated by dividing the MMA of the octadecanoic-d_{35} acid monolayer by the MMA of the octadecanol-d_{37} monolayer at 40 mN/m, and this ratio is then multiplied into the octadecanoic-d_{35} acid spectral peak intensities. As a result, the spectra of both fatty compounds have equivalent surface coverage for direct comparison of peak intensities. The scaling factors are plotted in Figure S2, and all octadecanoic-d_{35} acid spectra have been scaled.

The influence of the polar headgroup on the hydration shell as a function of temperature is not fully understood, especially at high number densities and at monolayer surfaces. For dilute solutions of water-soluble alcohols, the influence of the alcohol headgroup on the OH stretching region is negligible.[7] The alcohol OH stretch becomes significant at higher concentrations upon alcohol aggregation (greater than ~2.7 M for *tert*-butyl alcohol and *n*-propanol), meaning that the alcohol OH stretch is difficult, if not impossible, to separate from that of the water OH stretching modes. As a result, Deng et al. instead conducted their analysis on the HOH bending mode to isolate the contribution from water alone, but the water molecules solvating the headgroup versus surrounding the alkyl chain of the soluble alcohol could not be distinguished.[10]

IRRAS offers a unique advantage in that it only probes the monolayer and the hydration shell immediately perturbed by the presence of the fatty compounds at the interface; any signal from water molecules that matches the bare water surface reflectance will be subtracted from the reflectance−absorbance spectrum. Additionally, octadecanoic acid and octadecanol are highly insoluble, so their alkyl tails are directed toward and mostly exist in the air phase while only their polar headgroups are completely solvated within the water surface and subsurface region. Thus, we used IRRAS to spectrally probe the OH stretching (ν(OH), ~3000−3800 cm^{-1}) modes of the headgroups and their hydration shells as well as the HOH bending (δ(HOH), ~1500−1800 cm^{-1}) modes of the hydrating water molecules. We also probed the ν(OD) modes of dilute HOD to remove resonant vibrational excitation transfer, a Förster transfer mechanism mediated by transition dipole moment coupling; the ν(OD) modes thus act as uncoupled local modes for more reliable reporting of water structure.[27,28,82−87] All spectra were collected at 21.0 ± 0.5 and 1.0 ± 1.0 °C. Shifts in the OH and OD stretching region spectra as a function of temperature were quantified by Gaussian peak fitting (Figures S3, S4, S7, S8).

3.2.1. Fatty Alcohol Headgroup Hydration as a Function of Temperature. The OH (100% H_2O) and OD (10% HOD) stretching region spectra of octadecanol-d_{37} at 21.0 and 1.0 °C are plotted in parts a and b of Figure 2, respectively. For better visualization of the peak intensity changes, the Gaussian spectral deconvolutions at each temperature are plotted in Figures S3 and S4. Numerical values of the Gaussian peak fitted parameters are reported in Tables S2−S5. The ν(OH) and ν(OD) spectra have significantly different shapes. The ν(OH) region of the 100% H_2O subphase exhibits a two-peak structure (Figure 2a) and exhibits dramatically different spectral shifts with temperature; higher frequency regions of the ν(OH) spectra increase in peak intensity at low temperature, and the low frequency regions decrease in peak intensity. Thus, the intra- and intermolecular vibrational coupling mechanisms are likely highly sensitive to changes in temperature, resulting in the relative intensity shifts of the two main peaks in the OH stretching spectra. More specifically, changes in temperature alter the transition dipole moment strengths and hydrogen-bonding configurations of the interfacial water molecules, thereby shifting the distribution of resonant vibrational frequencies. Others have shown that an increase in temperature induces a frequency mismatch between the stretch fundamental and the bending overtone of bulk water, leading to a decrease in the Fermi resonance intramolecular coupling at ~3250 cm^{-1}.[88−92] Intramolecular coupling dominates the vibrational relaxation pathways in interfacial water.[86,93−95] Thus, intramolecular coupling is

https://doi.org/10.1021/acs.jpca.1c06101
J. Phys. Chem. A XXXX, XXX, XXX−XXX

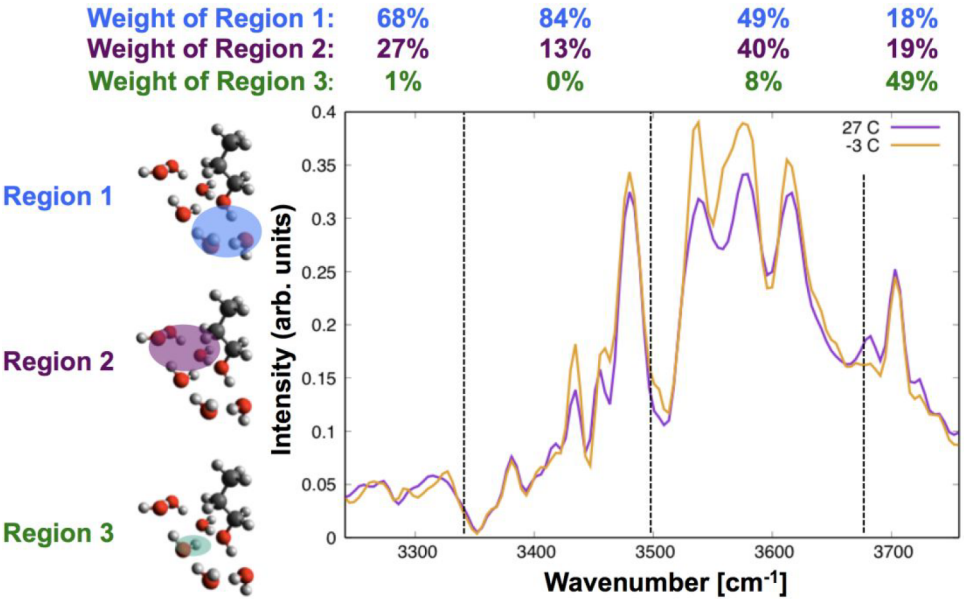

Figure 3. IR OH stretching region of propanol + $6H_2O$ at +27 and −3 °C. The dotted lines indicate natural changes in spectral features that correspond to shifts in the weights of correlated OH stretching motions that make up regions 1−3, shown on the left

possibly driving the temperature-dependent spectral shifts observed in Figure 2a, but the exact mechanisms responsible for these spectral shifts are currently unknown. Vibrational coupling to octadecanol-d_{37} vibrational modes is also possible.[96,97] Additionally, it is nontrivial to distinguish between peak intensity contributions caused by changes in hydration shell number density and structure versus changes in transition dipole moment strength as a function of temperature, further complicating the spectral interpretation. Consequently, calculations were performed that intrinsically include intra- and intermolecular coupling to study the contribution of transition dipole moments changes due to temperature for a single hydrogen-bonding configuration (Section 3.2.2).

In Figure 2b, the ν(OD) region of the 10% HOD spectrum contains a single peak. This decoupled spectral signature provides important insight into the hydrogen-bonding character of the hydration shell of the fatty acid and the fatty alcohol. As the temperature decreases to 1.0 °C, the ν(OD) spectrum red-shifts ∼10 cm^{-1}, indicating the formation of stronger hydrogen bonds with cooling, consistent with ice templating behavior for both the fatty acid and the fatty alcohol.

3.2.2. Ab Initio Molecular Dynamics (AIMD) Calculations and the Fundamental Vibrational Structure of IR Features. In order to gain insights into the temperature-dependent vibrational structure of the OH stretches of the headgroup and water molecules in the first solvation shell, AIMD calculations are performed on two model systems: propanol + $6H_2O$ and propionic acid + $10H_2O$. These systems are chosen to have a short, three-carbon chain to be sufficiently long that the water remains localized to the headgroup while keeping the system small for computational efficiency. One benefit of using cluster models is the ease with which internal coordinates (i.e., bond stretches, angle bends, and dihedral bends) can be defined for spectral decomposition. This allows for a detailed analysis of the hydrogen-bonding structure of the water molecules surrounding the headgroups as well as which molecular motions correspond with IR spectral features in the OH stretching region. While molecular dynamics studies have been performed on the changes in hydration structure around headgroups at monolayer interfaces, a study on the changes in vibrational structure and transition moments with temperature has not been conducted. In order to unravel the differences between changes in hydration structure and changes in transition moment, we turned to AIMD studies of model cluster systems.

Propanol + $6H_2O$ Cluster. The OH stretching region of the IR spectrum in the propanol + $6H_2O$ cluster is computed from AIMD calculations. The alcohol OH forms a donor hydrogen bond to water, which forms a four-membered ring (three H_2O and alcohol) that donates a hydrogen bond back to the alcohol. Using the spectral decomposition scheme described in Section 2.4 and the Supporting Information, we determine that three groupings of OH stretching motions, which we call regions 1−3, are highly correlated, as indicated in Figure 3. Region 1 is made up of three OH stretches: the alcohol OH stretch and two water OH stretches that form a chain coming from the alcohol OH stretch. Region 2 is made up of four water OH stretches in a ring with one stretch donating a hydrogen bond back to the OH of the alcohol. Finally, region 3 is a single water OH stretch by a water that donates a hydrogen bond to the alcohol OH. The spectral decomposition scheme determines that the IR spectrum can be broken up into four natural sections based on changes in the weights of these regions, shown with dotted lines in Figure 3 and described in detail in Figure S5. The OH stretches in region 1 contribute the most IR intensity to the spectrum between 3200 and 3674 cm^{-1}. However, the weight of region 2 is not negligible between 3200 and 3674 cm^{-1} and contributes 40% of the IR intensity (vs 49% from region 1) between 3496 and 3674 cm^{-1}. Between 3674 and 3757 cm^{-1}, the largest weight comes from region 3, the OH stretch donating a hydrogen bond to the alcohol OH, though regions 1 and 2 still contribute 18 and 19%, respectively. These spectral decomposition results highlight a key finding that localized groupings of highly correlated stretching motions underlie regions of large IR intensity in the OH stretching region.

https://doi.org/10.1021/acs.jpca.1c06101
J. Phys. Chem. A XXXX, XXX, XXX−XXX

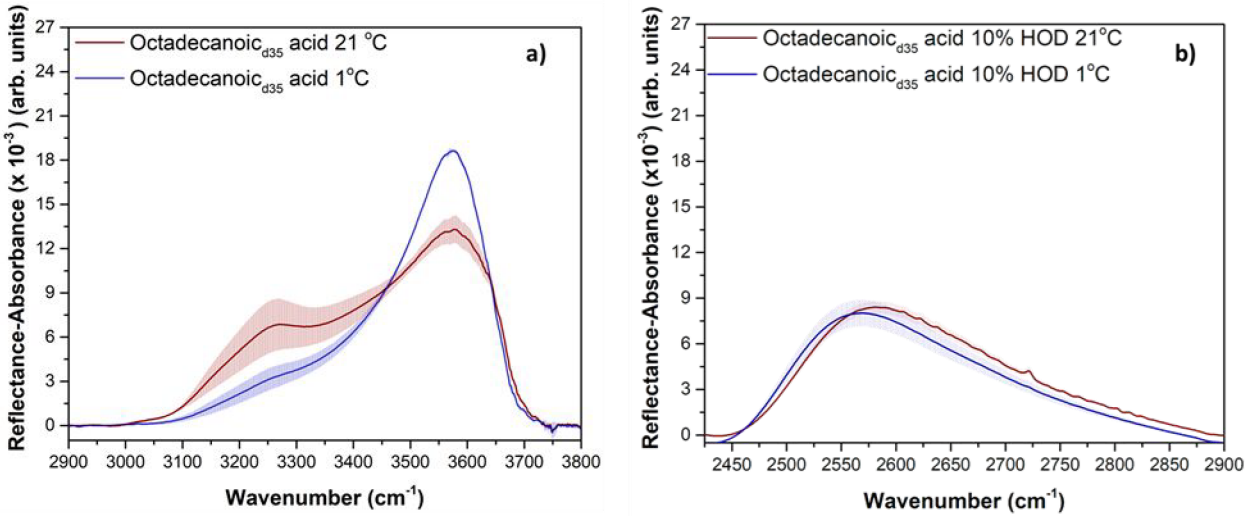

Figure 4. IRRAS spectra of the ν(OH) and ν(OD). (a) Octadecanoic-d_{35} acid illustrates the main ν(OH) bands one at 3600 cm^{-1}, typically attributed to the OH stretch of the groups weakly interacting with the neighbors and a 3250 cm^{-1} band due to strong interacting solvent (water) molecules at 21 °C ± 1 (red) and 1 °C ± 1(blue). (b) ν(OD) spectra region of octadecanoic-d_{35} acid in 5% D_2O in water (10% HOD). The OD and the OH oscillators are decoupled. The ν(OD) change in frequency as a function of temperature can be found in Table S6.

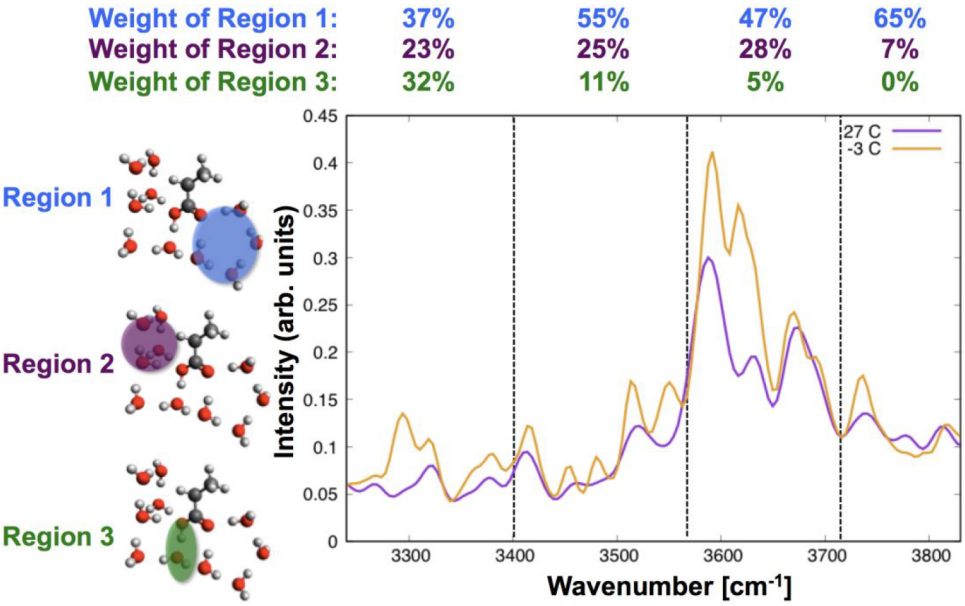

Figure 5. IR OH stretching region of propionic acid + 10H_2O at +27 and −3 °C. The dotted lines indicate natural changes in spectral features that correspond to shifts in the weights of correlated OH stretching motions that make up regions 1−3, shown on the left.

The effects of temperature on transition moment are computed as described in Section 2.4. This allows for an isolated study of the effects of temperature on changes in intensity, allowing for comparison to effects on intensity from changes in hydrogen-bonding structure at the monolayer interface, as described in Qiu et al.[3] We find that between 3460 and 3730 cm^{-1}, the intensities, on average, increase when the temperature lowers to −3 °C. At 3770 cm^{-1}, a feature corresponding to significant weight from region 3 appears that does not have significant change in intensity with respect to temperature. The OH stretching motions not highlighted do not have significant transition moments that contribute to the spectrum. In order to make a quantitative comparison between experimental and theoretical spectra, a Gaussian regression analysis was performed on the 27 °C and −3 °C spectra (Supporting Information). It is found that the decrease in temperature by 30 °C shifts the Gaussian peak to the red by 17 cm^{-1}, in agreement with the red shift seen in both the experimental H_2O and HOD stretching spectra. The decrease in temperature also increases spectral intensities, as seen in the higher frequency peak of the experimental H_2O stretching spectra corresponding to the first solvation shell. The experimental HOD stretching spectra show a decrease in intensity at lower temperatures. The computed spectra from AIMD inherently include intra- and intermolecular coupling that contributes to the unique spectral signatures of the octadecanol−H_2O interface and their temperature dependence. The red shift and intensity increase of the spectra from the propanol + 6H_2O cluster underline the role of intra- and intermolecular coupling in the higher frequency peak in the

https://doi.org/10.1021/acs.jpca.1c06101
J. Phys. Chem. A XXXX, XXX, XXX−XXX

OH stretching region of the H_2O−octadecanol interface, in contrast to the signatures of the HOD−octadecanol stretching region.

3.2.3. Fatty Acid Headgroup Hydration as a Function of Temperature. Changes in the OH (Figure 4a) and OD (Figure 4b) stretching regions of octadecanoic-d_{35} acid monolayers as a function of temperature resemble the trends observed for octadecanol-d_{37} monolayers in Figure 2a and 2b. Gaussian spectral deconvolutions at each temperature are plotted in Figures S7 and S8, and the numerical values of the fitted peak parameters are reported in Tables S2−S5. Like octadecanol-d_{37}, lowering the temperature from 21.0 to 1.0 °C also results in an ∼10 cm^{-1} red shift in the ν(OD) spectrum of the octadecanoic-d_{35} acid monolayer. The peak center frequencies are nearly identical for both monolayers held at the same temperature, suggesting that the hydrating water structure is quite similar between the two lipids. For the ν(OH) spectra, an increase in the high frequency region peak intensities near freezing matches the octadecanol-d_{37} spectral trends, although the peak intensity changes are not as large in magnitude for the octadecanoic-d_{35} acid monolayer. Suggesting that the intra- and intermolecular coupling mechanisms for interfacial water hydrating octadecanoic-d_{35} acid are weaker than the coupling mechanisms for water hydrating octadecanol-d_{37}. Consistent with the surface potential data (Figure 1), temperature has a smaller effect on octadecanoic acid monolayer organization and hydration structure.

Propionic Acid + 10H_2O Cluster. In comparing the OH stretching regions of the propanol + 6H_2O system and the propionic acid + 10H_2O system, the additional complexity of the carboxylic acid headgroup results in a more complex vibrational structure, shown in Figure 5. As found in the propanol + 6H_2O cluster, we determine that three groupings of OH stretching motions in the propionic acid + 10H_2O cluster, which we call regions 1−3, are highly correlated, as indicated in Figure 5. Region 1 is made up of five OH stretches from four water molecules forming a ring with two hydrogen bonds to the carboxylic acid ═O. Region 2 is made up of six water OH stretches in a four-water ring with two stretches donating a hydrogen bond to the OH of the carboxylic acid. Finally, region 3 consists of the OH stretch of the carboxylic acid and a water OH stretch that donates a hydrogen bond to a water molecule in region 1. The spectral decomposition scheme determines that the IR spectrum can be broken up into four natural sections based on changes in the weights of these regions, shown with dotted lines in Figure 5 and described in detail in the Supporting Information. The OH stretches in region 1 contribute the most IR intensity to the spectrum in the OH stretching region shown. However, the weight of region 2 is significant (23−28%) between 3240 and 3715 cm^{-1}. Region 3 contributes significant intensity between 3240 and 3401 cm^{-1}, but it quickly decreases in weight for higher frequencies and is not a major contributor (only 5%) to regions of large intensity between 3558 and 3715 cm^{-1}.

The effects of temperature on IR intensities are computed for the propionic acid + 10H_2O system. We find that in the OH stretching region, the IR intensities, on average, increase when the temperature lowers to −3 °C. As described for the propanol + 6H_2O cluster, a Gaussian regression analysis was performed on the +27 and −3 °C spectra, included in the Supporting Information. It is found that the decrease in temperature by 30 °C shifts the Gaussian peak to the red by 25 cm^{-1}, which agrees with the spectral shift found in the H_2O−octadecanoic acid and HOD−octadecanoic acid spectra. The decrease in temperature also increases spectral intensities, with the Gaussian peak increasing by 24%, modeling the behavior of the higher frequency peak in the H_2O−octadecanoic acid OH stretch region, which corresponds to the behavior of the first solvation shell. These findings, alongside the findings from the propanol + 6H_2O cluster spectra, strengthen our understanding of the role of intra- and intermolecular effects on the OH stretching region, which is further clarified via comparisons to the experimental HOD−octadecanoic acid stretching region spectra.

The vibrational structure of the model propanol + 6H_2O and propionic acid + 10H_2O systems provides insight into the effects of temperature on the transition moments. Because changes in IR intensity with temperature can be due to changes in hydrogen-bonding structure as well as changes in transition moment, studying such model systems provides this additional layer of complexity that has not been studied in previous dynamics studies of the changes in hydration at the monolayer surface in ice nucleation processes.[3,98−100] Furthermore, the decomposition of IR features from AIMD calculations provides deep insights into the correlation between individual OH stretches into natural groupings, and their contributions to IR features. In both model systems studied, the vibrations within different structural motifs contribute to markedly different IR features. As experimental tools continue to be developed for detection of markers for ice nucleation, predictions of spectral features and the molecular motions that contribute to them will be key to generating a fundamental picture of the chemical physics at play.

3.2.4. Water Bending Mode IRRAS Spectra as a Function of Temperature. The water bending mode in the IRRAS spectra provides a useful spectroscopic handle for selectively probing the headgroup hydration shell structure as a function of temperature.[101,102] Although the water bending mode is not as sensitive to the local molecular environment as the OH stretching region due to the smaller transition dipole moment, the water bending region is sufficiently isolated from the headgroup vibrational modes. Additionally, the HOH bending mode is devoid of intramolecular coupling, and intermolecular coupling of the bend vibration is considerably weaker than the stretch vibration, making the bending mode a reliable reporter of the hydration shell structure.[102−106] Figure 6 shows this spectroscopic region for the octadecanol-d_{37} (Figure 6a) and octadecanoic-d_{35} acid (Figure 6b) monolayers at room temperature and near freezing. At 21.0 °C, the water bending region is a positive band centered around ∼1665 cm^{-1}. The band red-shifts ∼18 cm^{-1} for the octadecanol-d_{37} monolayer and ∼21 cm^{-1} for the octadecanoic-d_{35} acid monolayer upon cooling to 1.0 °C. Red shifts in the water bending mode region indicate weakened intermolecular interactions within the hydration shell.[10,102,107] Additionally, the peak width increases with decreasing temperature for both compounds in the low frequency end of the spectrum, suggesting that the hydration shell is sampling a more heterogeneous hydrogen-bonding environment.

The small, albeit significant, temperature-dependent shift in the octadecanoic-d_{35} acid carbonyl stretching mode also provides evidence for the hydration structure (Figure 6). Cooling from 21.0 to 1.0 °C red-shifts the carbonyl mode by 4.5 cm^{-1} (Table S6), indicating that the intermolecular interactions between the headgroup and its surrounding environment increase near freezing. Consequently, this red

https://doi.org/10.1021/acs.jpca.1c06101
J. Phys. Chem. A XXXX, XXX, XXX−XXX

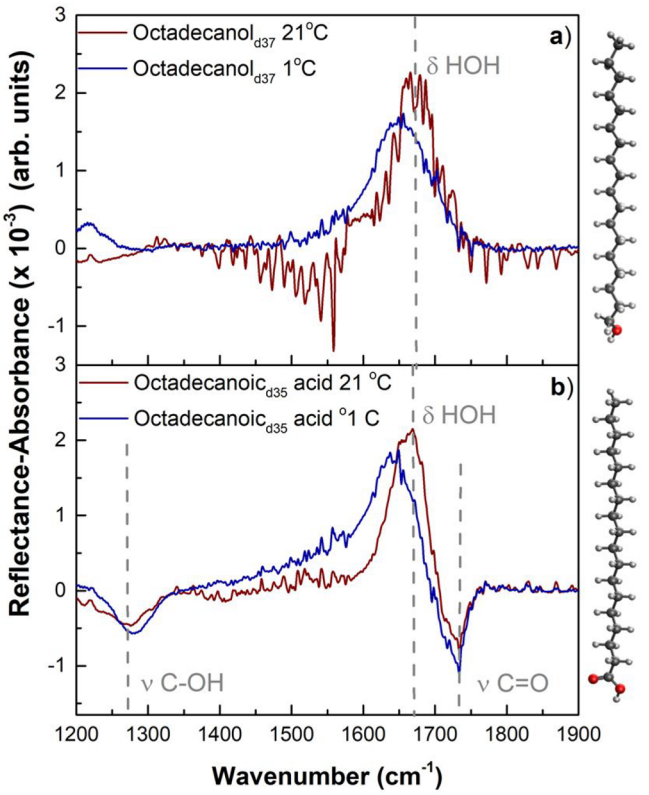

Figure 6. IRRAS spectra of the δ(OH) region of (a) Octadecanol-d_{37} (top), as well as (b) octadeconaoic-d_{35} acid (bottom) where we can also observe the ν(C═O) and ν(C−OH) regions. Changes in intensity as well as frequency are observed. The changes in frequency can be found in Table S6. Both parts a and b were recorded at 21 ± 1 (red) and 1 ± 1 °C (blue).

shift provides further spectral evidence that the hydrogen-bonding interactions between the headgroup and its hydration shell increase with decreasing temperature.

3.2.5. Evaluating the Spectral Impacts of Hydration Structure and Transition Dipole Moment Strength. The experimental OH stretching region IRRAS spectra of octadecanol-d_{37} and octadecanoic-d_{35} acid comprise a temperature-dependent convolution of hydration structure, differing transition dipole moment strengths, and intra- and intermolecular coupling. The AIMD calculations provide detailed molecular-level insights on the first hydration shell structure, and the calculations isolate the impacts of temperature on the transition dipole moment strengths. Both the experimental and computational spectra increase in intensity in the high frequency stretching regions at lower temperature, indicating that increasing transition dipole moments significantly enhance the 1.0 °C IRRAS spectral intensities for both fatty compounds. The higher frequency stretching regions are dominated by contributions from the first solvation shell around the fatty compound, allowing for comparisons between experiment and theory in these regions.

4. CONCLUSIONS

Through experiment and theory, we examine the temperature-dependent impacts of hydration structure and transition dipole moment strengths on the OH stretching region infrared reflection−absorption spectra of fatty alcohol and acid monolayers at the air−water interface. We also probe the decoupled OD of dilute HOD to isolate the effects vibrational excitation transfer observed in the pure H_2O data. We observe that temperature has a large impact on the intra- and intermolecular vibrational coupling between the octadecanol and octadecanoic acid headgroups and their hydration shells. We also find that changes in temperature affect the transition dipole moment strength, thus shifting the resonant vibrational frequency distributions. According to our surface pressure and surface potential−area isotherms, lowering the temperature promotes tighter packing. Monolayer compression to small surface area per molecule dehydrates the polar headgroups relative to the expanded monolayer at large areas per molecule, yielding a reduction in dipole moment screening between the headgroups. The infrared reflection−absorption ν(OH) spectra of these two compounds show two main OH stretching bands at 3600 and 3250 cm^{-1}, whereas the ν(OD) region contains a single peak at 2580 cm^{-1}. At low temperature the ν(OD) spectrum red-shifts, indicating the formation of stronger hydrogen bonds with cooling. Contrary, the ν(OH) reveals dramatically different spectral shifts. The higher frequency regions of the ν(OH) spectra increase in peak intensity at low temperature, whereas the low frequency regions decrease in peak intensity. We argue that intra- and intermolecular coupling dominates the vibrational relaxation pathways in interfacial water, thereby intramolecular coupling is more likely driving the temperature-dependent ν(OH) spectra shifts. Overall, the infrared reflection spectra suggest that temperature has a large impact on the intra- and intermolecular interactions between the headgroups and their hydration shells, and the octadecanol hydration shell. In the 10% HOD spectra, the ν(OD) mode is decoupled from the ν(OH) mode and reveal the behavior of the hydrogen-bonding network. We observed a significant red shift correlating ice templating behavior for both the fatty acid and the fatty alcohol. Moreover, our surface potential data corroborate prior observations of enhanced ice nucleating activity by long chain alcohols at the air−water interface.

Ab initio molecular dynamics (AIMD) simulations of propanol + 6H_2O and propionic acid + 10H_2O further reveal the effects of intra- and intermolecular coupling on the temperature-dependent transition dipole moment strengths in the OH stretching region spectra. For both the alcohol and the carboxylic acid, the overall calculated infrared spectral intensities increase with decreasing temperature due to enhanced transition dipole moment strengths. Thus, the increasing transition dipole moment strengths likely have a significant contribution to the increase in infrared reflection−absorption spectral peak intensities near freezing in the higher frequency stretching regions that represent the first solvation shell around the fatty compound. The cluster studies reveal the effects of the intra- and intermolecular coupling on the OH stretching region around the fatty compounds and simultaneously untangle the effects of cooling on the transition dipole moment strengths.

■ ASSOCIATED CONTENT

Supporting Information

The Supporting Information is available free of charge at https://pubs.acs.org/doi/10.1021/acs.jpca.1c06101.

Individual fatty alcohol and acid surface pressure and potential during compression, normalization plot used for IRRAS spectra as a function of temperature, based on

https://doi.org/10.1021/acs.jpca.1c06101
J. Phys. Chem. A XXXX, XXX, XXX−XXX

the MMA at 40 mN/m, and a table of MMA values used in categorizing of surface potential data (PDF)

AUTHOR INFORMATION

Corresponding Author

Heather C. Allen − *Department of Chemistry & Biochemistry, The Ohio State University, Columbus, Ohio 43210, United States;* orcid.org/0000-0003-3120-6784; Phone: +1-614-292-4707; Email: allen@chemistry.ohio-state.edu

Authors

Maria G. Vazquez de Vasquez − *Department of Chemistry & Biochemistry, The Ohio State University, Columbus, Ohio 43210, United States*

Kimberly A. Carter-Fenk − *Department of Chemistry & Biochemistry, The Ohio State University, Columbus, Ohio 43210, United States*

Laura M. McCaslin − *Combustion Research Facility, Sandia National Laboratories, Livermore, California 94551, United States*

Emma E. Beasley − *Department of Chemistry & Biochemistry, The Ohio State University, Columbus, Ohio 43210, United States*

Jessica B. Clark − *Department of Chemistry & Biochemistry, The Ohio State University, Columbus, Ohio 43210, United States*

Complete contact information is available at: https://pubs.acs.org/10.1021/acs.jpca.1c06101

Author Contributions

M.G.V.d.V. and E.E.B. collected all data. M.G.V.d.V. processed all experimental data. L.M.M. performed the AIMD calculations. J.B.C. assisted on data conceptualization and discussion. M.G.V.d,V., K.A.C.-F., and L.M. wrote and edited the manuscript. H.C.A. conceived of the experiment, supervised the project, and edited the manuscript.

Author Contributions

[§]M.G.V.d.V. and K.A.C.-F. contributed equally.

Notes

The authors declare no competing financial interest.

Data used to produce figures and conclusions in this manuscript are included in a Center for Aerosol Impacts of the Environment (CAICE) data set via USCD Library Digital Collections 10.6075/J05X2934.

ACKNOWLEDGMENTS

This research was funded by the National Science Foundation through the Center for Aerosols Impacts on Chemistry of the Environment, CAICE, under Grant No. CHE-1801971. We thank Prof. R. Benny Gerber for helpful discussion at the inception of this project. M.G.V.d.V. thanks Brian Vasquez and Mickey Rogers for their support throughout the development of this work. L.M.M. thanks Dr. Zeke Piskulich, Prof. Ward H. Thompson, and Dr. Timothy S. Zwier for helpful conversations and comments while developing this work. L.M.M. is supported by the Division of Chemical Sciences, Geosciences and Biosciences, Office of Basic Energy Sciences (BES), U.S. Department of Energy (USDOE). Sandia National Laboratories is a multimission laboratory managed and operated by National Technology and Engineering Solutions of Sandia, LLC., a wholly owned subsidiary of Honeywell International, Inc., for the U.S. Department of Energy's National Nuclear Security Administration under contract DE-NA-0003525. This paper describes objective technical results and analysis. Any subjective views or opinions that might be expressed in the paper do not necessarily represent the views of the U.S. Department of Energy of the United States Government.

REFERENCES

(1) Garrett, W. D. The Organic Chemical Composition of the Ocean Surface. *Deep-Sea Res. Oceanogr. Abstr.* **1967**, *14*, 221−227.

(2) DeMott, P. J.; Mason, R. H.; McCluskey, C. S.; Hill, T. C. J.; Perkins, R. J.; Desyaterik, Y.; Bertram, A. K.; Trueblood, J. V.; Grassian, V. H.; Qiu, Y.; et al. Ice Nucleation by Particles Containing Long-Chain Fatty Acids of Relevance to Freezing by Sea Spray Aerosols. *Environ. Sci. Processes Impacts* **2018**, *20*, 1559−1569.

(3) Qiu, Y.; Odendahl, N.; Hudait, A.; Mason, R.; Bertram, A. K.; Paesani, F.; DeMott, P. J.; Molinero, V. Ice Nucleation Efficiency of Hydroxylated Organic Surfaces Is Controlled by Their Structural Fluctuations and Mismatch to Ice. *J. Am. Chem. Soc.* **2017**, *139*, 3052−3064.

(4) Sharma, G.; Mohanty, K. K. Wettability Alteration in High-Temperature and High-Salinity Carbonate Reservoirs. *SPE J.* **2013**, *18*, 646−655.

(5) Serafin, A.; Figaszewski, Z. A.; Petelska, A. D. Phosphatidylcholine-Fatty Alcohols Equilibria in Monolayers at the Air/Water Interface. *J. Membr. Biol.* **2015**, *248*, 767−773.

(6) Tong, H.-J.; Yu, J.-Y.; Zhang, Y.-H.; Reid, J. P. Observation of Conformational Changes in 1-Propanol-Water Complexes by FTIR Spectroscopy. *J. Phys. Chem. A* **2010**, *114* (25), 6795−6802.

(7) Davis, J. G.; Gierszal, K. P.; Wang, P.; Ben-Amotz, D. Water Structural Transformation at Molecular Hydrophobic Interfaces. *Nature* **2012**, *491*, 582−585.

(8) Matvejev, V.; Zizi, M.; Stiens, J. Hydration Shell Parameters of Aqueous Alcohols: THz Excess Absorption and Packing Density. *J. Phys. Chem. B* **2012**, *116*, 14071−14077.

(9) Wu, X.; Lu, W.; Streacker, L. M.; Ashbaugh, H. S.; Ben-Amotz, D. Temperature-Dependent Hydrophobic Crossover Length Scale and Water Tetrahedral Order. *J. Phys. Chem. Lett.* **2018**, *9*, 1012−1017.

(10) Deng, G.-H.; Shen, Y.; Chen, H.; Chen, Y.; Jiang, B.; Wu, G.; Yang, X.; Yuan, K.; Zheng, J. Ordered-to-Disordered Transformation of Enhanced Water Structure on Hydrophobic Surfaces in Concentrated Alcohol-Water Solutions. *J. Phys. Chem. Lett.* **2019**, *10*, 7922−7928.

(11) Tuckerman, M. E.; Marx, D.; Parrinello, M. The Nature and Transport Mechanism of Hydrated Hydroxide Ions in Aqueous Solution. *Nature* **2002**, *417*, 925−929.

(12) Tuckerman, M.; Laasonen, K.; Sprik, M.; Parrinello, M. Ab Initio Molecular Dynamics Simulation of the Solvation and Transport of H3O+ and OH- Ions in Water. *J. Phys. Chem.* **1995**, *99*, 5749−5752.

(13) Robertson, W. H.; Diken, E. G.; Price, E. A.; Shin, J.-W.; Johnson, M. A. Spectroscopic Determination of the OH- Solvation Shell in the OH-·(H2O)n Clusters. *Science* **2003**, *299*, 1367−1372.

(14) Robertson, W. H.; Johnson, M. A. Molecular Aspects of Halide Ion Hydration: The Cluster Approach. *Annu. Rev. Phys. Chem.* **2003**, *54*, 173−213.

(15) Buch, V.; Sigurd, B.; Devlin, J. P.; Buck, U.; Kazimirski, J. K. Solid Water Clusters in the Size Range of Tens-Thousands of H2O: A Combined Computational/Spectroscopic Outlook. *Int. Rev. Phys. Chem.* **2004**, *23*, 375−433.

(16) Buck, U.; Pradzynski, C. C.; Zeuch, T.; Dieterich, J. M.; Hartke, B. A Size Resolved Investigation of Large Water Clusters. *Phys. Chem. Chem. Phys.* **2014**, *16*, 6859−6871.

(17) Fujii, A.; Sugawara, N.; Hsu, P.-J.; Shimamori, T.; Li, Y.-C.; Hamashima, T.; Kuo, J.-L. Hydrogen Bond Network Structures of Protonated Short-Chain Alcohol Clusters. *Phys. Chem. Chem. Phys.* **2018**, *20*, 14971−14991.

(18) Sun, T.; Ben-Amotz, D.; Wyslouzil, B. E. The Freezing Behavior of Aqueous N-Alcohol Nanodroplets. *Phys. Chem. Chem. Phys.* **2021**, *23*, 9991−100005.
(19) Alper, H. E.; Bassolino-Klimas, D.; Stouch, T. R. The Limiting Behavior of Water Hydrating a Phospholipid Monolayer: A Computer Simulation Study. *J. Chem. Phys.* **1993**, *99*, 5547−5559.
(20) Tan, H.-S.; Piletic, I. R.; Riter, R. E.; Levinger, N. E.; Fayer, M. D. Dynamics of Water Confined on a Nanometer Length Scale in Reverse Micelles: Ultrafast Infrared Vibrational Echo Spectroscopy. *Phys. Rev. Lett.* **2005**, *94*, 057405.
(21) Piletic, I. R.; Moilanen, D. E.; Spry, D. B.; Levinger, N. E.; Fayer, M. D. Testing the Core/Shell Model of Nanoconfined Water in Reverse Micelles Using Linear and Nonlinear IR Spectroscopy. *J. Phys. Chem. A* **2006**, *110*, 4985−4999.
(22) Zhao, W.; Moilanen, D. E.; Fenn, E. E.; Fayer, M. D. Water at the Surfaces of Aligned Phospholipid Multibilayer Model Membranes Probed with Ultrafast Vibrational Spectroscopy. *J. Am. Chem. Soc.* **2008**, *130*, 13927−13937.
(23) Berkowitz, M. L.; Vácha, R. Aqueous Solutions at the Interface with Phospholipid Bilayers. *Acc. Chem. Res.* **2012**, *45*, 74−82.
(24) Berkowitz, M. L.; Bostick, D. L.; Pandit, S. Aqueous Solutions next to Phospholipid Membrane Surfaces: Insights from Simulations. *Chem. Rev.* **2006**, *106*, 1527−1539.
(25) Moilanen, D. E.; Fenn, E. E.; Wong, D.; Fayer, M. D. Water Dynamics in Large and Small Reverse Micelles: From Two Ensembles to Collective Behavior. *J. Chem. Phys.* **2009**, *131*, 014704.
(26) Moilanen, D. E.; Fenn, E. E.; Wong, D.; Fayer, M. D. Geometry and Nanolength Scales versus Interface Interactions: Water Dynamics in AOT Lamellar Structures and Reverse Micelles. *J. Am. Chem. Soc.* **2009**, *131*, 8318−8328.
(27) Auer, B. M.; Skinner, J. L. IR and Raman Spectra of Liquid Water: Theory and Interpretation. *J. Chem. Phys.* **2008**, *128*, 224511.
(28) Auer, B.; Kumar, R.; Schmidt, J. R.; Skinner, J. L. Hydrogen Bonding and Raman, IR, and 2D-IR Spectroscopy of Dilute HOD in Liquid D2O. *Proc. Natl. Acad. Sci. U. S. A.* **2007**, *104*, 14215−14220.
(29) Hare, D. E.; Sorensen, C. M. Raman Spectroscopic Study of Dilute HOD in Liquid H_2O in the Temperature Range - 31.5 to 160 °C. *J. Chem. Phys.* **1990**, *93*, 6954−6961.
(30) Hare, D. E.; Sorensen, C. M. Interoscillator Coupling Effects on the OH Stretching Band of Liquid Water. *J. Chem. Phys.* **1992**, *96*, 13−22.
(31) Chai, J.-D.; Head-Gordon, M. Long-Range Corrected Hybrid Density Functionals with Damped Atom-Atom Dispersion Corrections. *Phys. Chem. Chem. Phys.* **2008**, *10*, 6615−6620.
(32) Kendall, R. A.; Dunning, T. H.; Harrison, R. J. Electron Affinities of the First-row Atoms Revisited. Systematic Basis Sets and Wave Functions. *J. Chem. Phys.* **1992**, *96*, 6796−6806.
(33) Martyna, G. J.; Klein, M. L.; Tuckerman, M. Nosé-Hoover Chains: The Canonical Ensemble via Continuous Dynamics. *J. Chem. Phys.* **1992**, *97*, 2635−2643.
(34) Shao, Y.; Gan, Z.; Epifanovsky, E.; Gilbert, A. T. B.; Wormit, M.; Kussmann, J.; Lange, A. W.; Behn, A.; Deng, J.; Feng, X.; et al. Advances in Molecular Quantum Chemistry Contained in the Q-Chem 4 Program Package. *Mol. Phys.* **2015**, *113*, 184−215.
(35) McQuarrie, D. A. *Statistical Mechanics*; Harper's chemistry series; Harper & Row: New York, 1975.
(36) Mathias, G.; Baer, M. D. Generalized Normal Coordinates for the Vibrational Analysis of Molecular Dynamics Simulations. *J. Chem. Theory Comput.* **2011**, *7*, 2028−2039.
(37) DeVine, J. A.; Debnath, S.; Li, Y.-K.; McCaslin, L. M.; Schöllkopf, W.; Neumark, D. M.; Asmis, K. R. Infrared Photodissociation Spectroscopy of D2-Tagged CH3CO2-(H2O)0−2 Anions. *Mol. Phys.* **2020**, *118*, No. e1749953.
(38) Wilson, E. B.; Decius, J. C.; Cross, P. C. *Molecular Vibrations: The Theory of Infrared and Raman Vibrational Spectra*; McGraw-Hill: New York, 1955.
(39) Piskulich, Z. A.; Thompson, W. H. Temperature Dependence of the Water Infrared Spectrum: Driving Forces, Isosbestic Points, and Predictions. *J. Phys. Chem. Lett.* **2020**, *11*, 7762−7768.
(40) Butt, H.-J.; Graf, K.; Kappl, M. *Physics and Chemistry of Interfaces*; John Wiley & Sons: 2013.
(41) Perkins, R. J.; Vazquez de Vasquez, M. G.; Beasley, E. E.; Hill, T. C. J.; Stone, E. A.; Allen, H. C.; DeMott, P. J. Relating Structure and Ice Nucleation of Mixed Surfactant Systems Relevant to Sea Spray Aerosol. *J. Phys. Chem. A* **2020**, *124*, 8806−8821.
(42) Valdes-Covarrubias, M. A.; Cadena-Nava, R. D.; Vasquez-Martinez, E.; Valdez-Perez, D.; Ruiz-Garcia, J. Crystallite Structure Formation at the Collapse Pressure of Fatty Acid Langmuir Films - IOPscience. *J. Phys.: Condens. Matter* **2004**, *16*, S2097−S2107.
(43) Oliveira, O. N., Jr; Bonardi, C. The Surface Potential of Langmuir Monolayers Revisited. *Langmuir* **1997**, *13*, 5920−5924.
(44) Bois, A. G.; Ivanova, M. G.; Panaiotov, I. I. Marangoni Effect and Relaxations of Surface Potential in Pentadecanoic Acid and Octadecanol Monolayers. *Langmuir* **1987**, *3*, 215−217.
(45) Kang, Y. S.; Lee, D. K.; Kim, Y. S. A Study on Temperature Dependency and in Situ Observation of Domain Structure in Langmuir Layers of Stearic Acid/γ-Fe2O3 Nanoparticle Complex at the Air/Water Interface. *Synth. Met.* **2001**, *117*, 165−167.
(46) Taylor, D. M.; Bayes, G. F. Calculating the Surface Potential of Unionized Monolayers. *Phys. Rev. E: Stat. Phys., Plasmas, Fluids, Relat. Interdiscip. Top.* **1994**, *49*, 1439−1449.
(47) Oliveira, O. N.; Taylor, D. M.; Lewis, T. J.; Salvagno, S.; Stirling, C. J. M. Estimation of Group Dipole Moments from Surface Potential Measurements on Langmuir Monolayers. *J. Chem. Soc., Faraday Trans. 1* **1989**, *85*, 1009.
(48) Oliveira, O. N.; Taylor, D. M.; Morgan, H. Modelling the Surface Potential-Area Dependence of a Stearic Acid Monolayer. *Thin Solid Films* **1992**, *210−211*, 76−78.
(49) Taylor, D. M.; De Oliveira, O. N.; Morgan, H. Models for Interpreting Surface Potential Measurements and Their Application to Phospholipid Monolayers. *J. Colloid Interface Sci.* **1990**, *139*, 508−518.
(50) Boyd, G. E. Energy Relations in Monolayer Formation: The Spreading of Long-Chain Fatty Acids on Aqueous Surfaces. *J. Phys. Chem.* **1958**, *62*, 536−541.
(51) Bernett, M. K.; Jarvis, N. L.; Zisman, W. A. Properties of Monolayers of -Monohalogenated Fatty Acids and Alcohols Adsorbed on Water. *J. Phys. Chem.* **1964**, *68*, 3520−3529.
(52) Lo Nostro, P.; Gabrielli, G. Temperature and Subphase Effects on Aliphatic Alcohol Films at the Air-Water Interface. *Langmuir* **1993**, *9*, 3132−3137.
(53) Gericke, A.; Huehnerfuss, H. In Situ Investigation of Saturated Long-Chain Fatty Acids at the Air/Water Interface by External Infrared Reflection-Absorption Spectrometry. *J. Phys. Chem.* **1993**, *97*, 12899−12908.
(54) Linden, D. J. M.; Peltonen, J. P. K.; Rosenholm, J. B. Adsorption of Some Multivalent Transition-Metal Ions to a Stearic Acid Monolayer. *Langmuir* **1994**, *10*, 1592−1595.
(55) Carter-Fenk, K. A.; Allen, H. C. Collapse Mechanisms of Nascent and Aged Sea Spray Aerosol Proxy Films. *Atmosphere* **2018**, *9*, 503.
(56) Can, S. Z.; Mago, D. D.; Walker, R. A. Structure and Organization of Hexadecanol Isomers Adsorbed to the Air/Water Interface. *Langmuir* **2006**, *22*, 8043−8049.
(57) Gaines, G. L. *Insoluble Monolayers at Liquid-Gas Interfaces*; Interscience Publishers: New York, 1966.
(58) Nutting, G. C.; Harkins, W. D. Pressure–Area Relations of Fatty Acid and Alcohol Monolayers. *J. Am. Chem. Soc.* **1939**, *61*, 1180−1187.
(59) Fischer, A.; Sackmann, E. Electron Microscopy and Electron Diffraction Study of Coexisting Phases of Pure and Mixed Monolayers Transferred onto Solid Substrates. *J. Colloid Interface Sci.* **1986**, *112*, 1−14.
(60) Adams, E. M.; Allen, H. C. Palmitic Acid on Salt Subphases and in Mixed Monolayers of Cerebrosides: Application to Atmospheric Aerosol Chemistry. *Atmosphere* **2013**, *4*, 315−336.
(61) Vogel, V.; Möbius, D. Local Surface Potentials and Electric Dipole Moments of Lipid Monolayers: Contributions of the Water/

https://doi.org/10.1021/acs.jpca.1c06101
J. Phys. Chem. A XXXX, XXX, XXX−XXX

Lipid and the Lipid/Air Interfaces. *J. Colloid Interface Sci.* **1988**, *126*, 408−420.
(62) Brockman, H. Dipole Potential of Lipid Membranes. *Chem. Phys. Lipids* **1994**, *73*, 57−79.
(63) Nakahara, H.; Nakamura, S.; Nakamura, K.; Inagaki, M.; Aso, M.; Higuchi, R.; Shibata, O. Cerebroside Langmuir Monolayers Originated from the Echinoderms: I. Binary Systems of Cerebrosides and Phospholipids. *Colloids Surf., B* **2005**, *42*, 157−174.
(64) Casper, C. B.; Verreault, D.; Adams, E. M.; Hua, W.; Allen, H. C. Surface Potential of DPPC Monolayers on Concentrated Aqueous Salt Solutions. *J. Phys. Chem. B* **2016**, *120*, 2043−2052.
(65) Shimoaka, T.; Tanaka, Y.; Shioya, N.; Morita, K.; Sonoyama, M.; Amii, H.; Takagi, T.; Kanamori, T.; Hasegawa, T. Surface Properties of a Single Perfluoroalkyl Group on Water Surfaces Studied by Surface Potential Measurements. *J. Colloid Interface Sci.* **2016**, *483*, 353−359.
(66) Adel, T.; Ng, K. C.; Vazquez de Vasquez, M. G.; Velez-Alvarez, J.; Allen, H. C. Insight into the Ionizing Surface Potential Method and Aqueous Sodium Halide Surfaces. *Langmuir* **2021**, *37*, 7863−7874.
(67) Van Vleet, E. S.; Williams, P. M. Surface Potential and Film Pressure Measurements in Seawater Systems. *Limnol. Oceanogr.* **1983**, *28*, 401−414.
(68) Yazdanian, M.; Yu, H.; Zografi, G.; Kim, M. W. Divalent Cation-Stearic Acid Monolayer Interactions at the Air/Water Interface. *Langmuir* **1992**, *8*, 630−636.
(69) Porter, E. F. Monomolecular Films of α-Aminostearic Acid, Stearic Acid, and Heptadecylamine. *J. Am. Chem. Soc.* **1937**, *59*, 1883−1888.
(70) Gericke, A.; Mendelsohn, R. Partial Chain Deuteration as an IRRAS Probe of Conformational Order of Different Regions in Hexadecanoic Acid Monolayers at the Air/Water Interface. *Langmuir* **1996**, *12*, 758−762.
(71) Gericke, A.; Huehnerfuss, H.; Michailov, A. V. Infrared Absorption-Reflection Spectroscopy of Long Chain Alcohols at the Air-Water Interface. *Proc. SPIE* **1991**, *1575*, 554−556.
(72) Mendelsohn, R.; Brauner, J. W.; Gericke, A. External Infrared Reflection Absorption Spectrometry of Monolayer Films at the Air-Water Interface. *Annu. Rev. Phys. Chem.* **1995**, *46*, 305−334.
(73) Flach, C. R.; Gericke, A.; Mendelsohn, R. Quantitative Determination of Molecular Chain Tilt Angles in Monolayer Films at the Air/Water Interface: Infrared Reflection/Absorption Spectroscopy of Behenic Acid Methyl Ester. *J. Phys. Chem. B* **1997**, *101*, 58−65.
(74) Flach, C. R.; Mendelsohn, R.; Rerek, M. E.; Moore, D. J. Biophysical Studies of Model Stratum Corneum Lipid Monolayers by Infrared Reflection-Absorption Spectroscopy and Brewster Angle Microscopy. *J. Phys. Chem. B* **2000**, *104*, 2159−2165.
(75) Mendelsohn, R.; Mao, G.; Flach, C. R. Infrared Reflection-Absorption Spectroscopy: Principles and Applications to Lipid-Protein Interaction in Langmuir Films. *Biochim. Biophys. Acta, Biomembr.* **2010**, *1798*, 788−800.
(76) Dote, J. L.; Mowery, R. L. Infrared Reflectance-Absorption Spectra of Langmuir-Blodgett Stearic Acid Monolayers on Gold and Aluminum: Influence of Substrate. *J. Phys. Chem.* **1988**, *92*, 1571−1575.
(77) Adams, E. M.; Casper, C. B.; Allen, H. C. Effect of Cation Enrichment on Dipalmitoylphosphatidylcholine (DPPC) Monolayers at the Air-Water Interface. *J. Colloid Interface Sci.* **2016**, *478*, 353−364.
(78) Adams, E. M.; Wellen, B. A.; Thiraux, R.; Reddy, S. K.; Vidalis, A. S.; Paesani, F.; Allen, H. C. Sodium-Carboxylate Contact Ion Pair Formation Induces Stabilization of Palmitic Acid Monolayers at High PH. *Phys. Chem. Chem. Phys.* **2017**, *19*, 10481−10490.
(79) Neal, J. F.; Zhao, W.; Grooms, A. J.; Flood, A. H.; Allen, H. C. Arginine-Phosphate Recognition Enhanced in Phospholipid Monolayers at Aqueous Interfaces. *J. Phys. Chem. C* **2018**, *122*, 26362−26371.
(80) Wellen Rudd, B. A.; Vidalis, A. S.; Allen, H. C. Thermodynamic versus Non-Equilibrium Stability of Palmitic Acid Monolayers in Calcium-Enriched Sea Spray Aerosol Proxy Systems. *Phys. Chem. Chem. Phys.* **2018**, *20*, 16320−16332.
(81) Denton, J. K.; Kelleher, P. J.; Johnson, M. A.; Baer, M. D.; Kathmann, S. M.; Mundy, C. J.; Wellen Rudd, B. A.; Allen, H. C.; Choi, T. H.; Jordan, K. D. Molecular-Level Origin of the Carboxylate Head Group Response to Divalent Metal Ion Complexation at the Air-Water Interface. *Proc. Natl. Acad. Sci. U. S. A.* **2019**, *116*, 14874−14880.
(82) Gaffney, K. J.; Piletic, I. R.; Fayer, M. D. Orientational Relaxation and Vibrational Excitation Transfer in Methanol-Carbon Tetrachloride Solutions. *J. Chem. Phys.* **2003**, *118* (5), 2270−2278.
(83) Corcelli, S. A.; Skinner, J. L. Infrared and Raman Line Shapes of Dilute HOD in Liquid H2O and D2O from 10 to 90 °C. *J. Phys. Chem. A* **2005**, *109*, 6154−6165.
(84) Yang, M.; Skinner, J. L. Signatures of Coherent Vibrational Energy Transfer in IR and Raman Line Shapes for Liquid Water. *Phys. Chem. Chem. Phys.* **2010**, *12*, 982−991.
(85) Yang, M.; Li, F.; Skinner, J. L. Vibrational Energy Transfer and Anisotropy Decay in Liquid Water: Is the Förster Model Valid? *J. Chem. Phys.* **2011**, *135*, 164505.
(86) Zheng, R.; Wei, W.; Sun, Y.; Song, K.; Shi, Q. Theoretical Study of Vibrational Energy Transfer of Free OH Groups at the Water-Air Interface. *J. Chem. Phys.* **2016**, *144*, 144701.
(87) Woutersen, S.; Bakker, H. J. Resonant Intermolecular Transfer of Vibrational Energy in Liquid Water. *Nature* **1999**, *402*, 507−509.
(88) Lock, A. J.; Bakker, H. J. Temperature Dependence of Vibrational Relaxation in Liquid H2O. *J. Chem. Phys.* **2002**, *117*, 1708−1713.
(89) Kraemer, D.; Cowan, M. L.; Paarmann, A.; Huse, N.; Nibbering, E. T. J.; Elsaesser, T.; Miller, R. J. D. Temperature Dependence of the Two-Dimensional Infrared Spectrum of Liquid H2O. *Proc. Natl. Acad. Sci. U. S. A.* **2008**, *105*, 437−442.
(90) Ramasesha, K.; De Marco, L.; Mandal, A.; Tokmakoff, A. Water Vibrations Have Strongly Mixed Intra- and Intermolecular Character. *Nat. Chem.* **2013**, *5*, 935−940.
(91) Hunter, K. M.; Shakib, F. A.; Paesani, F. Disentangling Coupling Effects in the Infrared Spectra of Liquid Water. *J. Phys. Chem. B* **2018**, *122*, 10754−10761.
(92) Kananenka, A. A.; Skinner, J. L. Fermi Resonance in OH-Stretch Vibrational Spectroscopy of Liquid Water and the Water Hexamer. *J. Chem. Phys.* **2018**, *148*, 244107.
(93) Sovago, M.; Campen, R. K.; Wurpel, G. W. H.; Müller, M.; Bakker, H. J.; Bonn, M. Vibrational Response of Hydrogen-Bonded Interfacial Water Is Dominated by Intramolecular Coupling. *Phys. Rev. Lett.* **2008**, *100*, 173901.
(94) Ishiyama, T. Energy Relaxation Path of Excited Free OH Vibration at an Air/Water Interface Revealed by Nonequilibrium Ab Initio Molecular Dynamics Simulation. *J. Chem. Phys.* **2021**, *154*, 104708.
(95) Ishiyama, T. Energy Relaxation Dynamics of Hydrogen-Bonded OH Vibration Conjugated with Free OH Bond at an Air/Water Interface. *J. Chem. Phys.* **2021**, *155*, 154703.
(96) Fischer, T. L.; Wagner, T.; Gottschalk, H. C.; Nejad, A.; Suhm, M. A. A Rather Universal Vibrational Resonance in 1:1 Hydrates of Carbonyl Compounds. *J. Phys. Chem. Lett.* **2021**, *12*, 138−144.
(97) Jiang, S.; Su, M.; Yang, S.; Wang, C.; Huang, Q.-R.; Li, G.; Xie, H.; Yang, J.; Wu, G.; Zhang, W.; et al. Vibrational Signature of Dynamic Coupling of a Strong Hydrogen Bond. *J. Phys. Chem. Lett.* **2021**, *12* (9), 2259−2265.
(98) Hudait, A.; Moberg, D. R.; Qiu, Y.; Odendahl, N.; Paesani, F.; Molinero, V. Preordering of Water Is Not Needed for Ice Recognition by Hyperactive Antifreeze Proteins. *Proc. Natl. Acad. Sci. U. S. A.* **2018**, *115*, 8266−8271.
(99) Lupi, L.; Hanscam, R.; Qiu, Y.; Molinero, V. Reaction Coordinate for Ice Crystallization on a Soft Surface. *J. Phys. Chem. Lett.* **2017**, *8*, 4201−4205.
(100) Lupi, L.; Peters, B.; Molinero, V. Pre-Ordering of Interfacial Water in the Pathway of Heterogeneous Ice Nucleation Does Not

https://doi.org/10.1021/acs.jpca.1c06101
J. Phys. Chem. A XXXX, XXX, XXX−XXX

Lead to a Two-Step Crystallization Mechanism. *J. Chem. Phys.* **2016**, *145*, 211910.
(101) Seki, T.; Sun, S.; Zhong, K.; Yu, C.-C.; Machel, K.; Dreier, L. B.; Backus, E. H. G.; Bonn, M.; Nagata, Y. Unveiling Heterogeneity of Interfacial Water through the Water Bending Mode. *J. Phys. Chem. Lett.* **2019**, *10*, 6936−6941.
(102) Seki, T.; Chiang, K.-Y.; Yu, C.-C.; Yu, X.; Okuno, M.; Hunger, J.; Nagata, Y.; Bonn, M. The Bending Mode of Water: A Powerful Probe for Hydrogen Bond Structure of Aqueous Systems. *J. Phys. Chem. Lett.* **2020**, *11*, 8459−8469.
(103) Bakker, H. J.; Skinner, J. L. Vibrational Spectroscopy as a Probe of Structure and Dynamics in Liquid Water. *Chem. Rev.* **2010**, *110*, 1498−1517.
(104) Ni, Y.; Skinner, J. L. IR and SFG Vibrational Spectroscopy of the Water Bend in the Bulk Liquid and at the Liquid-Vapor Interface, Respectively. *J. Chem. Phys.* **2015**, *143*, 014502.
(105) Dutta, C.; Benderskii, A. V. On the Assignment of the Vibrational Spectrum of the Water Bend at the Air/Water Interface. *J. Phys. Chem. Lett.* **2017**, *8*, 801−804.
(106) Yu, C.-C.; Chiang, K.-Y.; Okuno, M.; Seki, T.; Ohto, T.; Yu, X.; Korepanov, V.; Hamaguchi, H.; Bonn, M.; Hunger, J.; et al. Vibrational Couplings and Energy Transfer Pathways of Water's Bending Mode. *Nat. Commun.* **2020**, *11*, 5977.
(107) Zelent, B.; Nucci, N. V.; Vanderkooi, J. M. Liquid and Ice Water and Glycerol/Water Glasses Compared by Infrared Spectroscopy from 295 to 12 K. *J. Phys. Chem. A* **2004**, *108*, 11141−11150.

https://doi.org/10.1021/acs.jpca.1c06101
J. Phys. Chem. A XXXX, XXX, XXX−XXX